Applied Surface Science 481 (2019) 747–760

Contents lists available at ScienceDirect

Applied Surface Science

journal homepage: www.elsevier.com/locate/apsusc

Full length article

Syngas for Fischer-Tropsch synthesis by methane tri-reforming using nickel supported on $MgAl_2O_4$ promoted with Zr, Ce and Ce-Zr

Ananda Vallezi Paladino Lino[a,*], Yormary Nathaly Colmenares Calderon[b], Valmor Roberto Mastelaro[b], Elisabete Moreira Assaf[c], José Mansur Assaf[a]

[a] Universidade Federal de São Carlos, Depto. de Engenharia Química, Rod. Washington Luis km 235, São Carlos, SP, Brazil
[b] Instituto de Física de São Carlos, Departamento de Física e Ciências dos Materiais, Av. Trabalhador São-Carlense, 400, São Carlos, SP, Brazil
[c] Instituto de Química de São Carlos, Universidade de São Paulo, Av. Trabalhador São-Carlense, 400, São Carlos, SP, Brazil

ARTICLE INFO

Keywords:
Magnesium aluminate
Nickel catalyst
Zirconia
Ceria
Methane tri-reforming

ABSTRACT

Nickel catalysts supported on magnesium aluminate promoted with ZrO_2, $CeZrO_2$ and CeO_2 were evaluated under methane tri-reforming reaction. $MgAl_2O_4$ synthesis was assisted by P123® surfactant, assuring high porosity. The catalysts were tested at 650 °C and 750 °C. Zr and Ce−Zr promoted catalysts showed less coke deposition and increased conversions, mainly at 750 °C, while the non-promoted catalyst featured lowest reactants conversion due to an unstable performance caused by filamentous coke deposition. The H_2/CO ratio produced at 750 °C was at around 2, suitable to FT synthesis. *In situ* XPD analysis suggested nickel remained active as Ni^0 throughout the reaction, even in the oxidant environment, containing water and oxygen, and high-temperature exposure. Considering that nickel oxidation during the process is one of the concerns related to the catalyst deactivation during tri-reforming of methane, along with carbon deposition, these catalysts are promising to active and stable syngas production.

1. Introduction

Dry Reforming of Methane (DRM, reaction (1)) has gained a lot of interest in the last few years as a syngas (CO + H_2) producing route, once it consumes CH_4 and CO_2, both greenhouse gases. Furthermore, the H_2/CO ratio is more appropriate for fuel production by Fischer-Tropsch process than by Steam Reforming of Methane (SRM, reaction (2)) [1,2].

Song and Pan [3] studied the Tri-Reforming of Methane (TRM) aiming at minimizing the problems associated to DRM and SRM, which are related to carbon deposition, leading to catalyst deactivation and to the high energy consumption envolved, since both reactions are highly endothermic. According to them, integrating DRM and SRM with Partial Oxidation of Methane (POM, reaction (3)) in TRM process could drastically reduce the carbon deposition, produced according to reactions (4) to (6). Moreover, adequate amounts of O_2 in the feed allow *in situ* energy generation, due to the methane oxidation, making TRM more energy efficient.

TRM:

DRM $$CH_4 + CO_2 \rightarrow 2H_2 + 2CO \quad \Delta H^0_{298K} = +247.3\ kJ/mol \quad (1)$$

SRM $$CH_4 + H_2O \rightarrow 3H_2 + CO \quad \Delta H^0_{298K} = +206.3\ kJ/mol \quad (2)$$

POM $$CH_4 + \frac{1}{2}O_2 \rightarrow 2H_2 + CO \quad \Delta H^0_{298K} = -30.6\ kJ/mol \quad (3)$$

Carbon formation reactions

Methane decomposition: $$CH_4 \rightarrow C + 2H_2 \quad \Delta H^0_{298K} = +74.9\ kJ/mol \quad (4)$$

Boudoard reaction: $$2CO \rightarrow C + 2CO_2 \quad \Delta H^0_{298K} = -172.2\ kJ/mol \quad (5)$$

Syngas transformation: $$H_2 + CO \rightarrow C + H_2O \quad \Delta H^0_{298K} = -131.4\ kJ/mol \quad (6)$$

Changing reactants composition during TRM implies the versatility

* Corresponding author.
E-mail addresses: anandapaladino@gmail.com (A.V.P. Lino), yncolmenares@gmail.com (Y.N. Colmenares Calderon), valmor@ifsc.usp.br (V.R. Mastelaro), eassaf@iqsc.usp.br (E.M. Assaf), mansur@ufscar.br (J.M. Assaf).

https://doi.org/10.1016/j.apsusc.2019.03.140
Received 7 November 2018; Received in revised form 25 February 2019; Accepted 14 March 2019
Available online 15 March 2019
0169-4332/

of the produced syngas, being suitable for several applications [2,4].

The main catalysts requirements for TRM process are high specific surface area, thermal stability, coke deposition resistance and economic viability [5]. Jiang and coauthors [6] studied nickel catalysts supported on magnesia, titania and solid solutions produced from MgO and TiO_2 combination. They suggested the catalysts must have a good reducibility cycle in order to keep nickel phase always available as metallic species, since Ni^0 can be oxidized by O_2 and water and insert in the MgO lattice, which is facilitated by the high reaction temperature, causing the catalyst deactivation [6].

Considering the catalysts requirements described previously, the $MgAl_2O_4$ spinel was chosen as the nickel catalyst support for the TRM reaction. Nickel catalysts supported on $MgAl_2O_4$ are known to be sintering resistant due to the strong interaction between the active phase and the support. They also feature a high specific surface area and thermal stability at high temperature, which minimize the support sintering. The metallic dispersion stability is also better than other supports, like ZrO_2 and CeO_2, which usually feature a low specific surface area and sintering tendency. Additionally, $MgAl_2O_4$ spinel shows basicity properties that avoid or minimize the coke production [7,8]. For all these features, they are extensively applied to SRM and DRM.

ZrO_2 [9] and $CeZrO_2$ mixed oxides [5] are usually reported as the support for the nickel catalysts used in TRM process, which can be associated to other base metal, as Mg [5]. The main drawback of zirconia is low stability at high temperatures [8]. Despite the combination of CeO_2 and ZrO_2 oxides improves the properties of the individual oxides, as oxygen storage and mobility, and the redox properties, the low specific surface area of the combined oxides and sintering tendency are the main limitations for application to the reforming reactions at high temperature [8,10]. Moreover, these oxides are expensive, which may difficult their acquisition [10].

Despite a great number of reports of nickel catalysts supported on magnesium aluminate applied to DRM and SRM and oxidative reforming processes, such catalyst has yet to be studied on the TRM. Thus, the aim of this work was to evaluate Ni catalysts supported on $MgAl_2O_4$ during tri-reforming of methane. Besides, Zr and Ce + Zr were added in the support in order to study the effects on the catalytic performance. Debek and coauthors [11] showed that zirconia in nickel-based catalysts derived from Mg—Al hydrotalcites makes carbon gasification easier. According to Shin and coauthors [12], ZrO_2 minimizes the carbon deposition on the Ni/Al_2O_3 catalyst during DRM by improving CO_2 adsorption, followed by the dissociation to CO and O species, due to acid-base properties. Ce improved the $Ni/MgAl_2O_4$, leading to higher nickel dispersion over the spinel support, increasing the reducibility at lower temperatures and decreasing the coke formation compared to non-promoted catalyst during the combined Steam and Dry Reforming of Methane [13]. In DRM, $CeZrO_2$ allowed the carbon gasification for Ni/Al_2O_3 catalyst, due to the oxygen mobility in the solid solution [14]. CeO_2 and ZrO_2 also facilitate NiO species activation, ensuring their reducibility [15], making ever-available nickel species for the reactants adsorption.

2. Experimental

2.1. Catalyst preparation

3.6692 g of P123 Pluronic® (Sigma-Aldrich, MM = 5800) was dissolved in 100 mL of deionized water and kept at vigorous stirring for 24 h. The P123®/(Mg^{+2} + Al^{+3}) molar ratio was 0.01. After surfactant solubilization, stoichiometric amounts of $Mg(NO_3)_2{\cdot}6H_2O$ (Sigma-Aldrich, 99%) and $Al(NO_3)_3{\cdot}9H_2O$ (Sigma-Aldrich, ≥ 98%) were added to the aqueous solution containing the surfactant. A 27% (w/w) ammonia solution added dropwise kept the pH at around 10.5 + −0.2. The mixture was stirred for 50 min, refluxed at 80 °C for 20 h under agitation, cooled down to room temperature and washed with deionized water. The slurry obtained was dried at 100 °C for 1 day and calcined in air flow (100 mL·min^{-1}). Calcination was carried out in two steps: 1) the sample was heated from room temperature to up to 500 °C (2 °C·min^{-1}), and kept at this temperature for 1 h for surfactant removal; and 2), it was heated to up to 750 °C (5 °C·min^{-1}) and kept at this temperature for 4 h. The support obtained was named MA.

A support was also prepared without the surfactant for comparison. It was designated as 'MA without P123®' in the Textural Properties section.

The incipient impregnation technique was used in the preparation of Zr, Zr + Ce and Ce promoted supports. $ZrO(NO_3)_2.6H_2O$ (99%, Aldrich), $Ce(NO_3)_3{\cdot}6H_2O$ (99%, Aldrich) or $ZrO(NO_3)_2{\cdot}6H_2O$ and Ce $(NO_3)_3{\cdot}6H_2O$, was dissolved in water at the proportion of 0.0011 mol of Zr, Zr + Ce (Zr/Ce molar ratio of 0.25) or Ce, per g of $MgAl_2O_4$. This proportion was calculated taking into consideration the cubic ZrO_2 (JCPDS-07-0337) monolayer coverage over MA support prepared using the surfactant, considering that its specific surface area was 170 m^2·g^{-1}. The aqueous solution containing the elements to be impregnated was dropped onto the support and mixed until incipient wetness was reached. Then, it was dried at 100 °C for 2 h. This step was repeated until all nitrate solution had been added to the spinel support. At the end of the impregnation, each promoted support was calcined at 750 °C (5 °C·min^{-1}) in air flow (100 mL·min^{-1}) for 4 h. The supports were named ZMA, CZMA and CMA.

Nickel was inserted also by incipient impregnation and calcined for 4 h at 750 °C (5 °C·min^{-1}) in air flow (100 mL·min^{-1}). The nominal active phase content in the final catalyst was adjusted to 10 wt%. The fresh catalysts designations were NMA, NZMA, NCZMA and NCMA.

2.2. Characterization

X-ray diffraction patterns were acquired in a Siemens D50005 equipment (CuKα radiation source, λ = 15,406 Å and 40 kV–15 mA) by powder method and 2θ range from 10° to 70° (step 0.02°).

In situ XPD was performed at the Brazilian Synchrotron Light Laboratory (Campinas-Brazil) in the XPD-10B beam line, with a Huber diffractometer, Arara furnace, Mythen detector and Si monochromator. Diffraction patterns were obtained in 2θ range from 10°to 70°.

Fresh and spent catalysts SEM analyses were performed using a Philips XL-30 FEG, coupled with an EDS accessory for chemical analysis. The samples were dispersed in isopropyl alcohol and dropped on a glass sample holder, covered with a gold grid.

The B.E.T. specific surface area was measured by N_2 physical adsorption at −196 °C in an ASAP 2020 — Micromeritics equipment. Average pore size distribution and pore volume were obtained from the isotherm desorption branch, using B.J.H. method.

Temperature programmed reduction with H_2 (TPR-H_2) was carried out in a Micromeritics Auto Chem II Chemisorption Analyzer using a U-shaped quartz reactor, and a 10% H_2/N_2 (v/v) mixture (30 mL·min^{-1}), from room temperature to 950 °C (5 °C·min^{-1}). Each sample (50 mg) was previously flushed with argon at 200 °C for 1 h.

Catalysts basicity was determined by CO_2 temperature programmed desorption (CO_2-TPD) using a Micromeritics Auto Chem II Chemisorption Analyzer. The fresh catalyst (approx. 57 mg) was heated from room temperature to 200 °C, and kept for 1 h in He flow (30 mL·min^{-1}). Then, it was reduced at 750 °C for 1 h in a 10% H_2/N_2 (v/v) mixture (20 mL·min^{-1}). After activation, it was cooled down (in He flux) to 45 °C, and exposed to pure CO_2 (30 mL·min^{-1}) for 10 min. After CO_2 chemisorption, the sample was purged with He for 1 h (30 mL·min^{-1}), and heated from room temperature to up to 750 °C (5 °C·min^{-1}) for CO_2 desorption.

The X-ray Photoemission Spectroscopy (XPS) was executed using a Scienta Omicron ESCA spectrometer system equipped with an X-ray Al k α (1486.7 eV) monochromated source and a EA125 hemispherical analyzer. Cn10 Omicron charge neutralizer with beam energy in 1.6 eV was used in order to compensate the samples charge and correct the

spectra charge effects. XPS spectra data treatment was made using the *Casa XPS* software, where the background in high-resolution spectra is computed by the Shirley method, and the charge effect is corrected using the C1s at 284.6 eV. Peak fitting was performed using a *Gaussian-Lorentzian* product function for peaks shape, while the peak area ratio between Zr $3d_{5/2}$ and Zr $3d_{3/2}$ peaks components was maintained.

2.3. Catalytic tests

Catalytic tests were carried out in a fixed bed quartz reactor with 85 mg of fresh catalyst (60–100 mesh) supported over quartz wool. Prior to each reaction, the sample was reduced *in situ* under H_2 flow (30 mL·min^{-1}) at 750 °C for 1 h.

CH_4, CO_2, H_2O and air (20% O_2/N_2) were fed to the reactor using 0.00210 mol·min^{-1} of CH_4 (51.5 NmL·min^{-1}), 0.0007 mol·min^{-1} of CO_2 (17.2 NmL·min^{-1}); 0.00035 mol·min^{-1} of O_2 (42.8 NmL·min^{-1} of air) and 0.001 mol·min^{-1} of water steam, which was pumped and then vaporized in a pre-heater chamber at 180 °C before reaching the reactor (1 CH_4:0.33 CO_2:0.47 H_2O:0.17 O_2 ratio). The runs were carried out at 650 °C and 750 °C.

Reactor effluents were analyzed in line using a Varian® 3800 GP gas chromatograph, equipped with 2 TCD and 3 columns: 2 Porapack®-N and a 13× molecular sieve. He and N_2 were the carrier gases. The unreacted water was collected in a condenser before the gas stream reached the chromatograph.

Catalytic performances were evaluated considering the CH_4 and CO_2 conversions (X_i, i = CH_4 or CO_2), and H_2 (Y_{H2}) and CO (Y_{CO}) yields, calculated using the following expressions:

$$X_i = \frac{Fi_{in} - Fi_{out}}{Fi_{in}}. 100\%$$

$$Y_{H2} = \frac{F_{H2}}{2F_{CH4\,in} + F_{H2O\,in}}. 100\%, \text{ in} = CH_4 \text{ or water fed to the reactor}$$

$$Y_{CO} = \frac{F_{CO}}{F_{CH4\,in} + F_{CO2\,in}}. 100\%, \text{ in} = CH_4 \text{ or } CO_2 \text{ fed to the reactor}$$

The amount of carbon deposited over the catalyst during the reaction tests per reaction hour was determined by thermogravimetric analysis (TGA) in an ATG-DTG 60H Shimadzu Simultaneous DTA-TG thermogravimetric analyzer.

Carbon deposits graphitization was evaluated by Raman spectroscopy in a Vitec α 300R (λ = 514.6 nm) equipment.

3. Results and discussion

3.1. XRD

Fig. 1a and b show the supports and fresh catalysts XRD patterns, respectively. Shoulders near 2θ = 43° and 63° in MA support pattern is related to MgO phase [7]. ZMA and CZMA supports also show additional peaks, related to the cubic and/or tetragonal zirconia phase. As reported by Youn and coauthors [16], it is not possible to distinguish the cubic zirconia from the tetragonal structure, since both feature quite similar position of the main peaks. Monoclinic zirconia (JCPDS-02-0536) was not detected. The CMA support presented the fluorite type structure related to the CeO_2 (JCPDS-01-0800).

As for the fresh catalysts patterns, the NiO was not observed as a separate phase, due to the overlapping of the peaks corresponding to NiO (JCPDS-78-0643) and $MgAl_2O_4$ spinel (JCPDS-21-1152).

Zirconia peaks for CZMA support and NCZMA fresh catalyst were slightly shifted towards lower angle than ZMA and NZMA, respectively, as highlighted by an approximation at 2θ = 25 to 35° range (Fig. 1c). It shows the zirconia lattice expansion, once Ce^{+4} (0.97 Å) is bigger than Zr^{+4} (0.84 Å) [16,17]. Additionally, it indicates the formation of a $CeZrO_2$ solid solution in the CZMA support, whose lattice parameter was 5.14 Å, a value expected by the Vegard's law [18], considering a molar ratio of Ce:Zr = 1:4 and taking into consideration that the lattice parameter of the ZrO_2 cubic phase was 5.05 Å in the ZMA and 5.40 Å in the CMA. From Fig. 1c, it was also noticed that nickel incorporation to the supports did not affect the CeO_2 and $CeZrO_2$ lattice parameters, except for the ZrO_2 phase in NZMA fresh catalyst, where it was observed a lattice expansion compared to the ZrO_2 phase in ZMA support (from 5.05 Å to 5.07 Å).

3.2. Textural properties

MA isotherm is graded as type II (Fig. 2a), according to IUPAC classification. The sharp increase in N_2 adsorption at high pressure is typical of macropores [19,20]. The hysteresis loop is classified as H3 type, due to the non-uniform size and slit-shaped pores (spaces among the platelets-like particles). The hysteresis loop at $P/P_0 > 0.85$ indicated that the mesopores were generated inside the macropore wall [19,21,22]. According to Lu and Liu [23], the smaller mesopores are associated to the inner pores of the particles, while the bigger pores due to the slits between the stacked particles. A similar result was obtained by Lee and coworkers [24], during the preparation of $LaMnO_3$ particles with P123®, where such meso/macropores pore network was attributed to the copolymer molecular nature itself. Once P123® is considered an amphiphilic tri-block copolymer and a non-anionic surfactant, its hydrophobic group (polypropylene oxide) can segregate into a hydrophobic phase, while its hydrophilic groups (polyethylene oxide) show more affinity to the metal hydroxides polar phase. Thus, the polyethylene oxide groups can adsorb on the surface of Mg and/or Al metal and be organized into hierarchic structure, where the smaller pores are produced inside the larger pores.

The other supports and fresh catalysts featured type IV isotherms (Fig. 2a).

The support prepared without the surfactant was reported to highlight the effect of the copolymer on the synthesis: it increased the pore volume, leading to a greater specific surface area, as shown in Table 1. Considering the catalysts were prepared with successive impregnations between the calcinations (first the promoters Zr, Ce + Zr or Ce, and then, the active phase, Ni), was clearly required a support with a higher porosity. Thus, all of the studies were made impregnating only the support with the surfactant, because this series would lead to better results, as once shown by Mustu and coworkers [25], which showed that the catalysts whose supports (ZrO_2) were prepared with the assistance of the P123® presented larger specific surface area and smaller average pore size, which lead to an active phase “confinement” effect and thus avoided the sintering of the nickel particles. In this present work the pore size was the same for both synthesis (MA and MA without surfactant), that let to suppose the increase of pore volume (porosity) can contribute to better disperse the active phase, once it lead to a higher specific surface area, and consequently, more space would be available to accommodate the active phase.

Specific surface area, porosity and pore size decreased with Zr, Zr + Ce and Ce addition. The pores larger than 25 nm disappeared (Fig. 2b), indicating the elements occupied these largest pores. The pore volume and pore size of the NMA, NZMA, NCZMA and NCMA were also lower than their respective supports, due to the nickel addition. The Ce incorporation on the MA support produced the largest average pore size among the promoted supports and the lowest value of the BET surface area, probably due to the non-porous nature of ceria [26].

3.3. H_2-TPR

The H_2 consumption curves of the supports are represented in Fig. S1 (Supplementary Material). According to Youn and coauthors [16], the surface reduction of pure ZrO_2 (Zr^{+4} to Zr^{+3}) happens at around 700 °C; bulk reduction, only above 1000 °C [5]. It is noticed a wide peak in ZMA support at around 500 °C, probably related to the reduction of

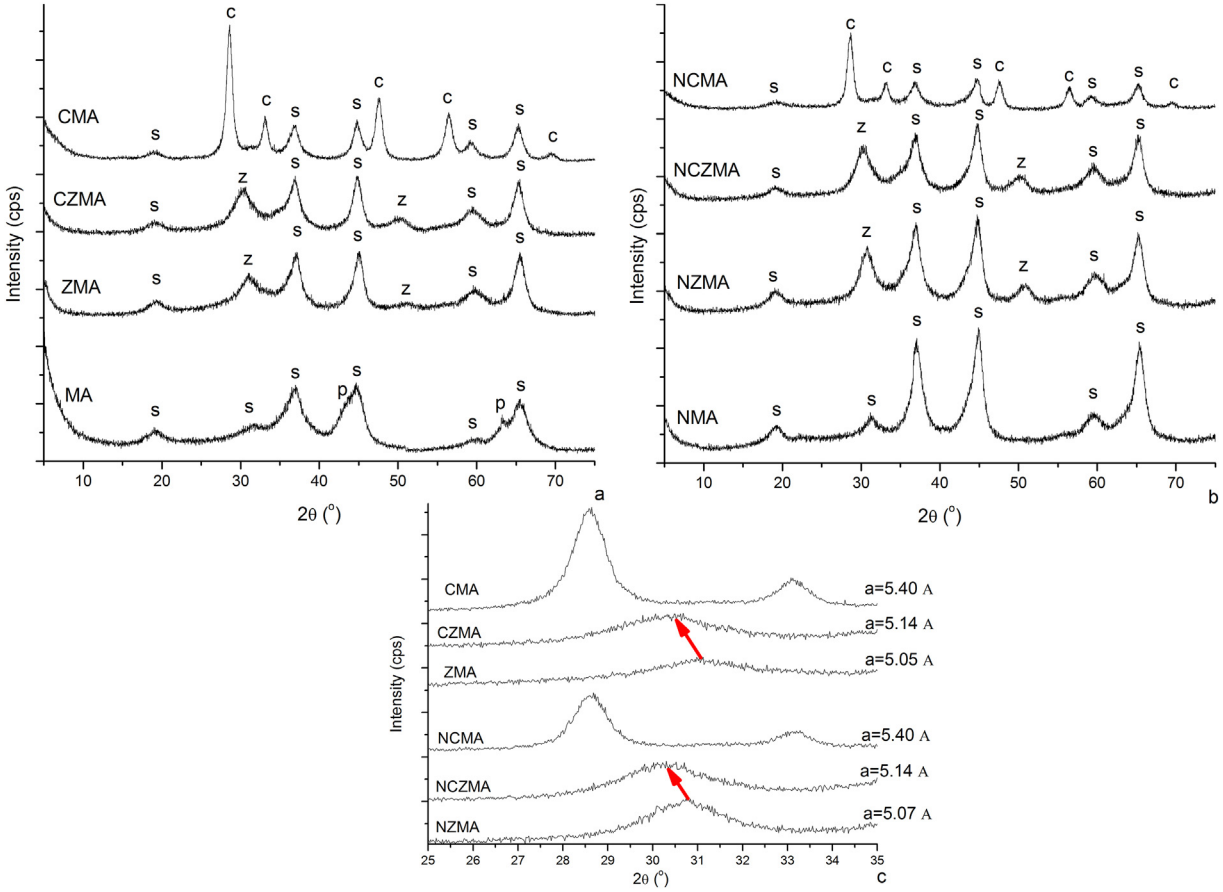

Fig. 1. Supports (a), fresh catalysts (b) XRD patterns and ZrO_2 (111) approximation (c); s—spinel, z—cubic and/or tetragonal zirconia, c—ceria.

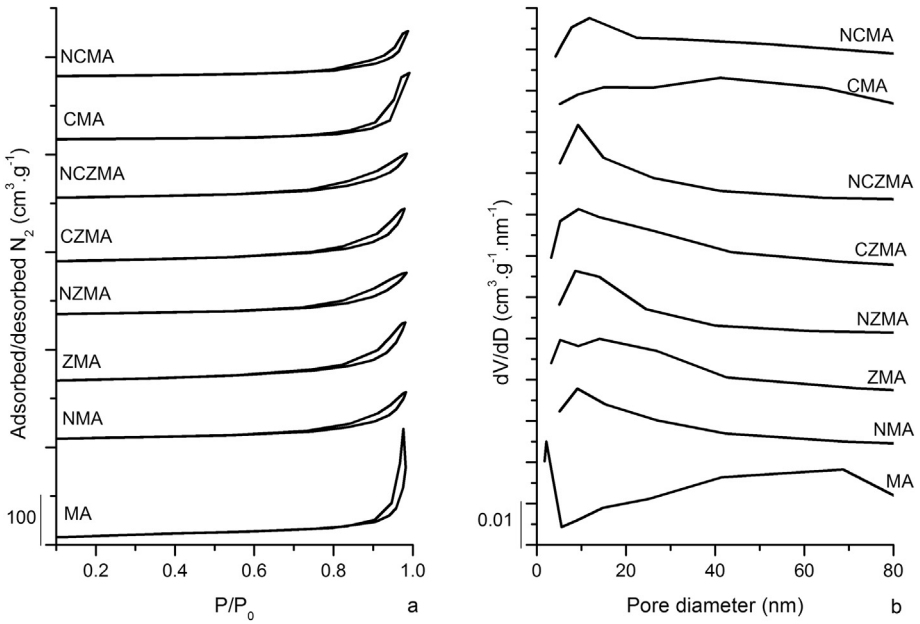

Fig. 2. N_2 isotherms (a) and pore size distribution (b).

the surface oxygen atoms that are shared by the zirconia-spinel interface. The CZMA support shows a peak at 400 °C, due to activation of ceria surface oxygen [3]. The CMA curve shows the surface ceria reduction up to 800 °C. It is observed a trend of peak formation, at temperatures higher than 800 °C, related to the reduction of the bulk ceria [14].

As for the fresh catalysts reduction curves (Fig. 3), there are distinct H_2 consumption zones, related to the strength of the interaction between nickel oxide and the support. The reduction of the oxygen adsorbed on the surface and/or NiO that interacts weakly with the support occur at the low temperature zone, *i.e.*, up to 400 °C [27,28]. NiO that interacts moderately with $MgAl_2O_4$ was reduced at 400 °C–600 °C

Table 1
Supports and fresh catalysts textural properties.

Sample	BET Specific surface area (± 10 $m^2 \cdot g^{-1}$)	Pore volume ($cm^3 \cdot g^{-1}$)	D_{pore} (nm)
MA without P123®	112	0.61	25.0
MA P123®	170	0.99	24.5
NMA	100	0.40	15.3
ZMA	124	0.50	14.3
NZMA	87	0.35	13.9
CZMA	120	0.46	14.9
NCZMA	91	0.37	14.0
CMA	89	0.50	19.0
NCMA	83	0.39	15.0

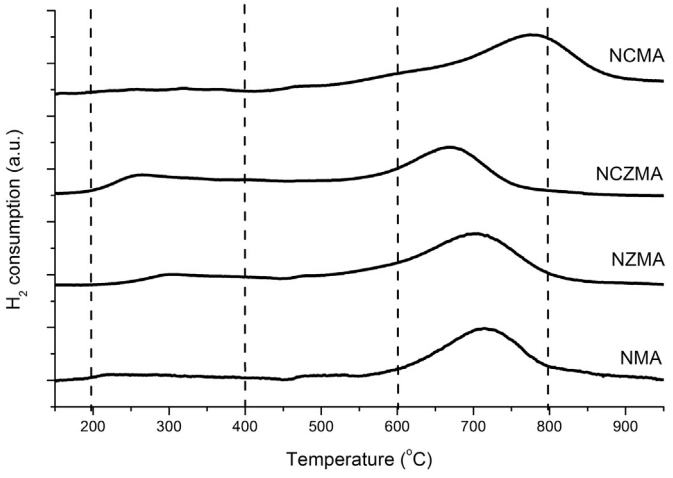

Fig. 3. Catalysts H_2-TPR.

range, while species with strong interaction are activated at 600 °C–800 °C [7,29,30]. All catalysts showed main reduction peaks above 600 °C, suggesting nickel oxide is dispersed on the support and develops strong interaction with the spinel [26]. Temperatures higher than 800 °C are required to activate stable species, as $(NiMg)Al_2O_4$ solid solution [7,32,33]. Except the NCMA fresh catalyst, none of the catalysts showed significant H_2 consumption above this temperature, suggesting the absence of such species. According to Eltejaei and coauthors [8], the overlapping of the peak related to the NiO reduction that shows strong interaction to the support and the surface reduction of Ce^{+4} to Ce^{+3} may have influenced on the NCMA main reduction peak displacement to higher temperature, once CMA support presented the tendency of a peak formation at temperature higher than 800 °C.

Nickel reduction was easier for NZMA and NCZMA catalysts, as the main reduction peak shifted to lower temperatures. Additionally, the relative proportions of NiO species that interact weakly (up to 400 °C) and moderately (400 °C–600 °C) with the support increased in these samples, as shows Table 2, which indicates the addition of Zr and Ce + Zr to the spinel support favored the NiO activation. The NCMA fresh catalyst presented the strongest metal-support interaction (SMSI), since almost 80% of the total H_2 consumption came from species that feature strong interaction with the spinel. Such SMSI can be caused by the presence of more dispersed particles. As will be shown in Table 5, the NCMA presented the lowest Ni^0 average size after the reduction process. Koo and coauthors [13] also found that Ce addition on the $MgAl_2O_4$ spinel increased the active phase dispersion.

Samples reduction was also examined by *in situ* XRD (Fig. S1). NiO reduction started at 585 °C, 620 °C, 655 °C and 690 °C (peaks at 2θ = 44° and 52°) in NCZMA, NZMA, NMA and NCMA catalysts, respectively, suggesting easier NiO reduction in presence of the Zr and Ce + Zr additives, which corroborates with H_2-TPR spectra.

The expected H_2 consumption shown in Table 2 considers that all nickel (calculated from EDX analysis) was completely reduced to Ni^0. The amount of H_2 consumed by nickel species for NMA, NCZMA and NCMA, which was obtained discounting the total amount of H_2 consumed by the catalyst from the H_2 consumed by the reducible additives in the spinel, was slightly higher than the expected, due to the spillover phenomenon [34].

3.4. XPS analysis

The surface composition determined by X-ray photoelectron spectroscopy (XPS) are compared with the atomic bulk composition measured by energy dispersive X-ray (EDX) in Table 3:

The fresh catalysts showed a Ni/Mg surface ratio lower than in the bulk, which means nickel species are at the inner layers of the catalysts. The NCMA showed the lowest Ni/Mg molar ratio in the surface among all the catalysts studied, due to the strongest interaction between NiO and the support, corroborating with the H_2-TPR analysis results. This catalyst also featured more Mg on its surface, *i.e.* the lowest Al/Mg surface ratio among the fresh catalysts. Such Mg excess can difficult the NiO reduction, due to solid solution formation between MgO and NiO in a non-stoichiometric spinel structure, leading to more dispersed particles [31], as observed in the previous H_2-TPR analysis.

The gradient of the zirconium concentration was more evident for ZMA support than for NZMA fresh catalyst. The difference between surface and bulk zirconium composition was less significant after the calcination of the ZMA support impregnated with nickel, suggesting the zirconia migration to the surface during the thermal treatment. A similar behavior was observed for Zr concentration in CZMA and NCZMA samples.

High-resolution XPS spectra for Mg 2p and Al 2p regions (Fig. 4) showed small changes in the curve shape and in the binding energy among the samples, indicating the absence of any $MgAl_2O_4$ chemical variation with the Zr, Zr + Ce and Ce addition.

The nickel, zirconium and cerium high-resolution spectra (Ni 2p3/2, Zr 3d and Ce 3d) were acquired in order to study the interaction among the added elements. Ni 2p3/2 core level binding energies (BE) in NMA, NZMA, NCZMA and NCMA fresh catalysts were 855.9, 855.6, 855.7 eV and 855.7 eV, respectively (Fig. 5), with a satellite peak at around 862 eV, related to the NiO presence. These values were higher than the theoretical NiO BE (854.2 eV) and similar to the BE reported for Ni_2O_3 (856 eV), $NiAl_2O_4$ (856 eV), NiO-MgO solid solution (855.7 eV) and (MgNi)AlO solid solution (855.5 eV) [35,36]. These higher BE are due to the electron transfer from nickel to magnesium and/or aluminum, resulting into the strong interaction between nickel and support, as shown in TPR results [36,37].

The shifts to lower Ni 2p3/2 binding energies observed for the NZMA and NCZMA fresh catalysts spectra compared to the NMA sample can be due to some electron transfer from the additives (Zr, in case of NZMA, and Zr and/or Ce, in case of NCZMA) to nickel. Thus, the shift of the main reduction peaks related to the H_2 consumption observed in the NZMA and NCZMA fresh catalysts, which was discussed in the previous section, was a consequence of the electron transfer from these additives to the nickel, due to the chemical disturbance around NiO caused by the additives incorporation. A shift to a lower Ni 2p3/2 binding energy was also observed in the NCMA fresh catalyst, due to the electronic transfer from Ce to Ni [26]. As also discussed in the H_2-TPR section, the SMSI observed in the case of the NCMA catalyst may result from the presence of higher dispersed particles and not from the electronic interaction between Ni and Ce, that was supposed to weaken the interaction between NiO and the support.

XPS spectra fitting for Zr 3d core levels (Fig. 6) shows zirconium in two oxidation states. Indeed, the Zr 3d5/2 level was fitted with peaks at 182.9 eV and 181.6 eV, which correspond to Zr^{+4} and Zr^{+x} states, respectively. Since Zr^{+x} peak binding energy is lower, it is possible to confirm that corresponds to zirconia in Zr^{+x} oxidation state, with

Table 2
TPR H_2 consumption.

Sample	H_2 consumption (± 5.0 µmol)	H_2 consumed by nickel species (± 5.0 µmol)	Amount of H_2 consumption expected considering all nickel is reduced to Ni^0 (± 5.0 µmol)*	Ni % wt (EDS)[1]	Nickel reducibility (%)	Weak (%)**	Moderate (%)**	Strong (%)**
MA	0	–	–	–	–	–	–	–
NMA	86.4	86.4	78	9.1 ± 0,8	100	4.0	32.4	63.6
ZMA	2.1	–	–	–	–	–	–	–
NZMA	82.8	80.7	88	10.4 ± 1,5	92	15.5	31.0	53.5
CZMA	3.4	–	–	–	–	–	–	–
NCZMA	75.0	71.6	68	8.0 ± 1,0	100	7.7	40.0	52.3
CMA	8.6	–	–	–	–	–	–	–
NCMA	96.1	87.5	78	8.8 ± 0,7	100	2.5	17.6	79.9

* Taking into account the $NiO + H_2 \rightarrow Ni^0 + H_2O$ reduction.
** Obtained by the deconvolution of the H_2 consumption curves.
[1] EDS measurements were carried out in six distinct regions of each sample.

Table 3
Relative atomic surface (XPS) and bulk (EDX) compositions and the Zr^{x+}/Zr^{+4} ratio.

Sample	Surface				Bulk				Zr^{+x}/Zr^{+4}
	Al/Mg	Ni/Mg	Zr/Mg	Ce/Mg	Al/Mg	Ni/Mg	Zr/Mg	Ce/Mg	
NMA	2.0	0.10	–	–	2.3	0.28	–	–	–
ZMA	1.8	–	0.09	–	2.1	–	0.20	–	2.81
NZMA	1.9	0.14	0.10	–	2.1	0.34	0.15	–	5.78
CZMA	1.7	–	0.05	0.02	2.3	–	0.18	0.05	3.33
NCZMA	1.9	0.11	0.09	0.02	2.3	0.28	0.16	0.04	3.08
CMA	1.5	–	–	0.01	1.7	–	–	0.12	–
NCMA	1.4	0.05	–	0.01	1.7	0.25	–	0.11	–

$0 < x < 4$ [38].

Fig. 6 and Table 3 showed that the Zr^{+x}/Zr^{+4} area ratio for NZMA fresh catalyst was higher than ZMA support. Ni^{+2} is a less positive cation than Zr^{+4} and its presence causes a disturbance around the Zr^{+4} environment, which led ZrO_2 to acquire an overall negative charge, as discussed by Youn and coauthors [16]. ZrO_2 releases oxygen and produces vacancies in order to keep its electron neutrality, explaining the participation increment of Zr^{+x} species, where x represents a positive charge lower than 4. The higher Zr^{+x}/Zr^{+4} ratio for NZMA fresh catalyst may explain the lattice expansion of ZrO_2 compared to ZMA support, as highlighted at $2\theta = 29–35^\circ$ in Fig. 1c at XRD results section, considering that Zr^{+x} with a charge lower than 4 is greater than Zr^{+4}. Shifts to higher Zr^{+4} binding energies are also observed in NZMA, which suggested an electron transfer from Zr to Ni.

The Zr BE for CZMA support was the same as for ZMA, while Zr^{x+}/Zr^{4+} ratio was nearly 18% greater than ZMA, maybe due to oxygen vacancies formation when Ce is associated to Zr.

The NCZMA Zr^{+x}/Zr^{+4} ratio was almost similar to CZMA. In fact, this ratio decreased from 3.33 (CZMA) to 3.08 (NCZMA), indicating higher Zr^{+4} content in the fresh catalyst. According to Pantaleo and coworkers [39], the interaction between NiO and CeO_2 creates defects in CeO_2 structure, releasing oxygen because of the vacancies produced from the Ni−Ce interaction. These released oxygen species could oxidize some Zr^{+x} to Zr^{+4}. This fact may also explain the absence of a shift in ZrO_2 NCZMA diffraction peak compared to CZMA support (Fig. 1c), distinctly of the observed for ZMA and NZMA.

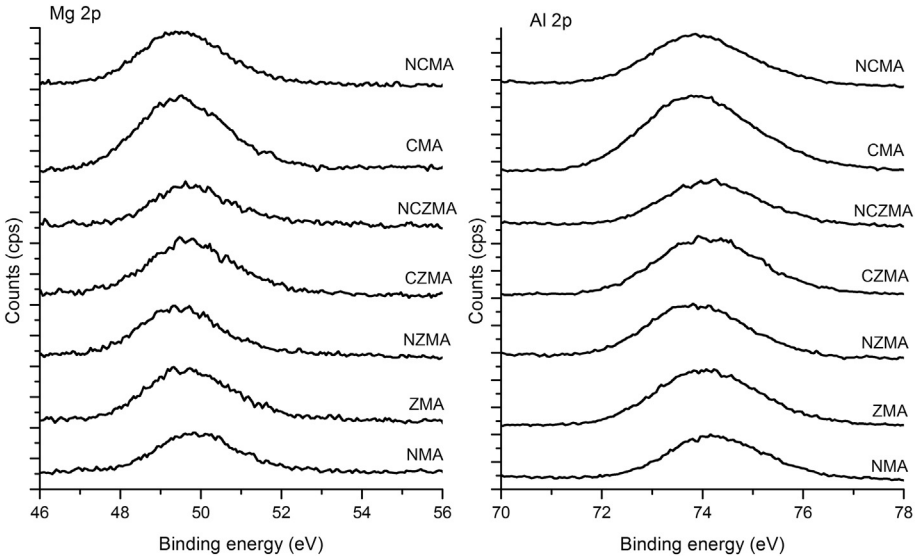

Fig. 4. Mg 2p and Al 2p XPS spectra.

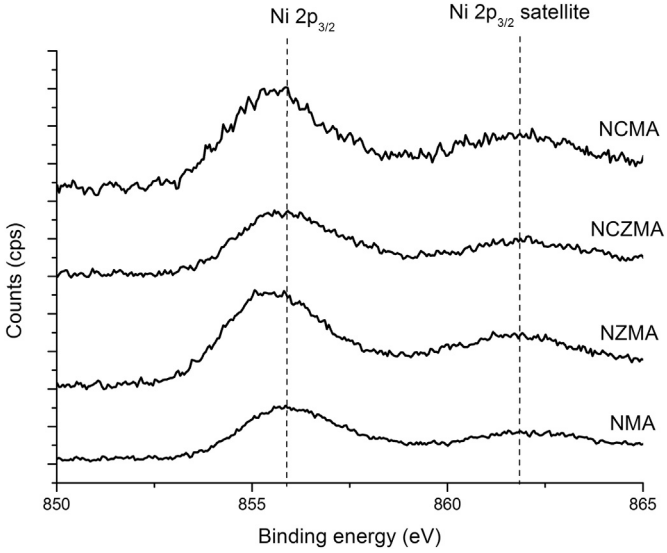

Fig. 5. Ni 2p3/2 level XPS analysis.

The presence of the peak in Ce 3d5/2 region (Fig. 7) at 882.4 eV for CZMA and 882.3 eV for CMA indicates that Ce is mainly in a Ce^{+4}oxidation, which is also supported by a satellite near to 917 eV, that is only present in Ce^{4} oxide state [40]. This binding energy value is higher than the reported in the literature for Ce 3d5/2 (881.8 eV), which in case of the CZMA support can indicate the electron transfer from Ce to Zr in the $CeZrO_2$ solid solution; as for the CMA, the electron transfer from Ce to the spinel support [41].

Since the Ce d5/2 and Ni p1/2 binding energies are close, it is difficult to determine the real position of the Ce d5/2 binding energy in NCZMA and NCMA samples, once nickel concentration is higher than cerium in these fresh catalysts.

From such XPS results, it can be said the presence of the additives Zr and Ce disturbs the chemical environment, especially around nickel, without necessarily producing a solid solution between NiO and the oxides of these elements, except in case of NZMA. The increase of the Zr^{+x} participation in NZMA was probably due to the incorporation of Ni^{+2} to the ZrO_2 lattice. In general, the changes in the Ni 2p3/2 binding energies among the samples studied are in the order of some tenths electron volts, indicating nickel oxide still develops a strong interaction with the support matrix, $MgAl_2O_4$, in all fresh catalysts.

3.5. Basicity properties

The complex CO_2 desorption profiles seen in Fig. 8 suggested base sites of different nature. Up to 150 °C, the base sites are graded as weak and related to the CO_2 desorption from hydroxyls groups. Desorption occurring at temperatures higher than 270 °C are related to strong base sites, where CO_2 molecules are adsorbed as unidentate carbonate on isolated O^{-2} anions. Temperatures ranging between 150 °C and 270 °C are associated to moderate sites, like metal-oxygen acid-base pairs [42,43].

NCZMA featured lower total basicity than NMA, while the total amount of NZMA base sites was slightly higher than the NMA catalyst (Table 4). Debek and coauthors [15] showed that Ce and Zr addition to Ni/Mg/Al hydrotalcite-derived catalyst reduced the total base sites compared to the non-promoted catalyst, probably due to the presence of separate promoter phases on the hydrotalcite-derived mixed oxides surface. In fact, the catalysts presented $CeZrO_2$ segregated phase on spinel, as discussed in the XRD section.

NCZMA basicity was also lower than in NZMA. Cutrufello and

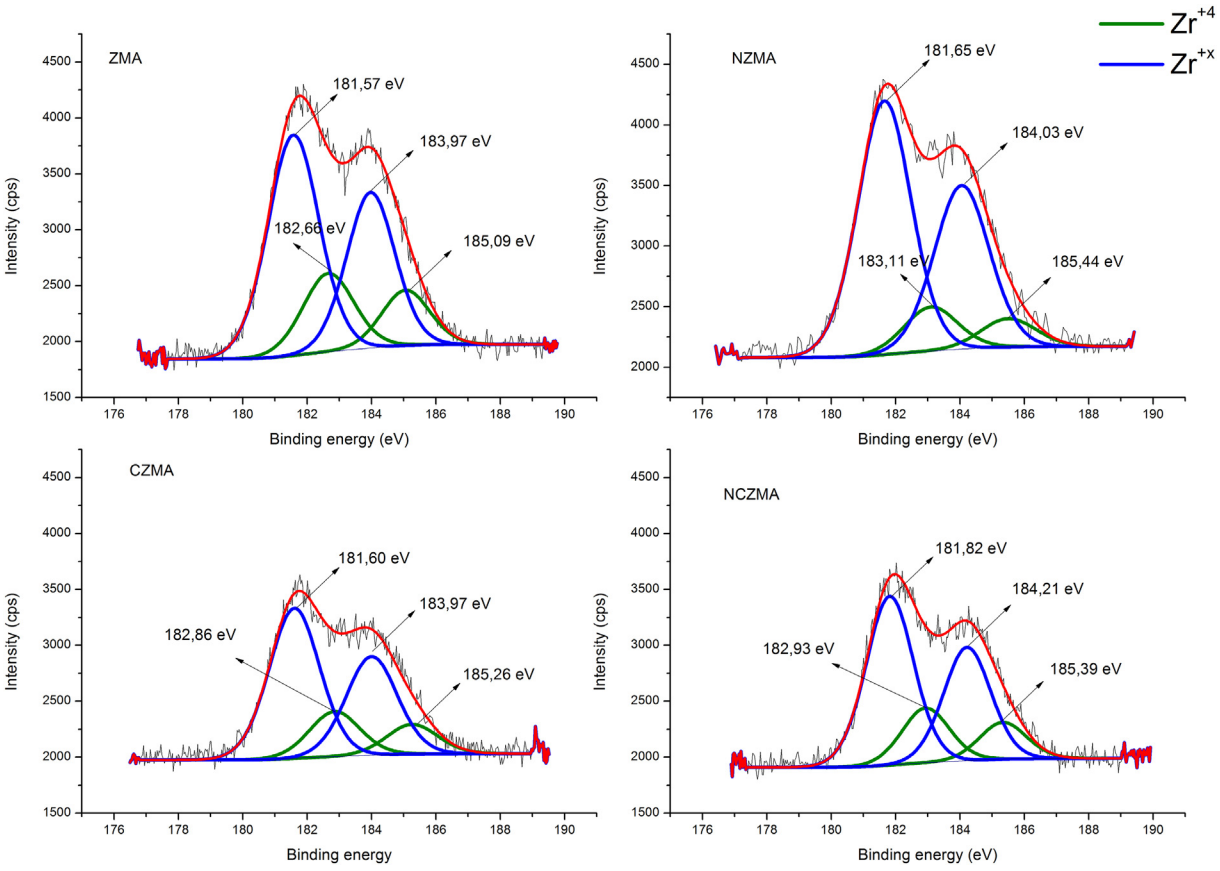

Fig. 6. Zr 3d level XPS analysis.

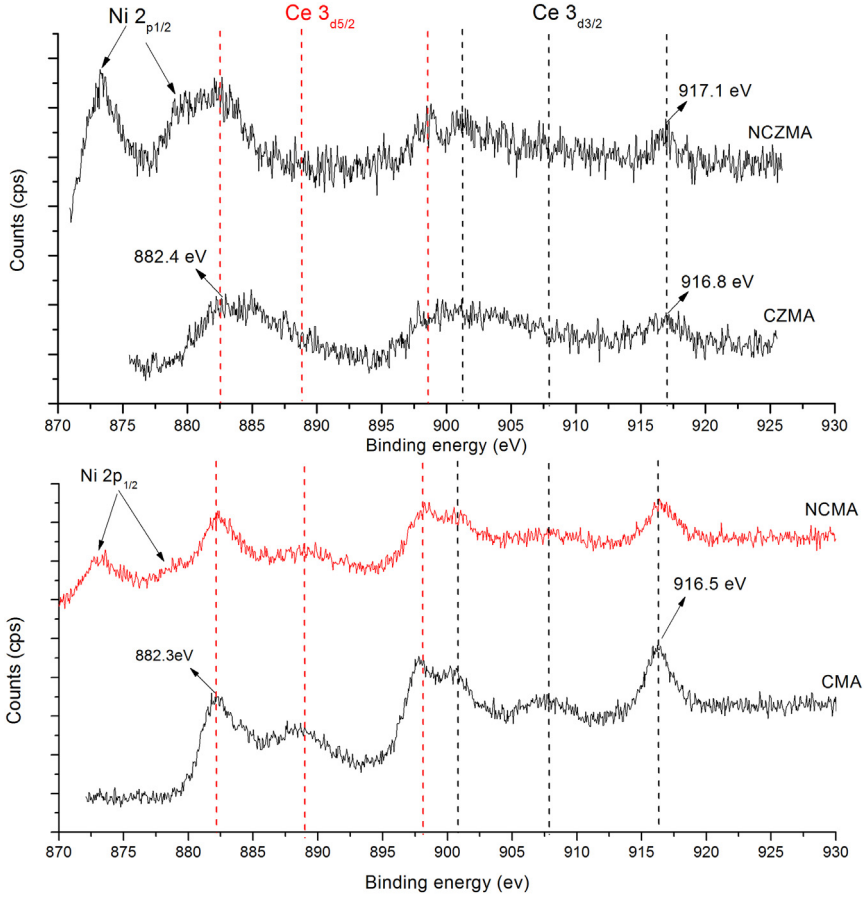

Fig. 7. Ce 3d level XPS analysis.

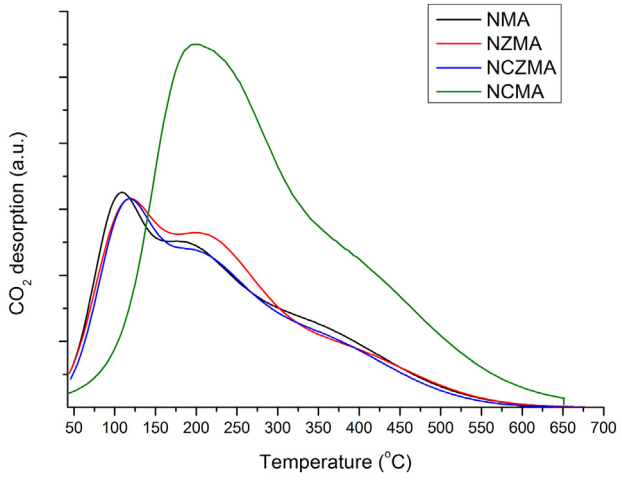

Fig. 8. Catalysts CO_2-TPD profile.

Table 4
Catalysts base properties.

Catalyst	Basicity mmol·g^{-1} (± 0.01)	Weak* %	Moderate* %	Strong* %
NMA	0.60	16.1	35.5	48.4
NZMA	0.62	21.9	50.0	28.1
NCZMA	0.56	20.7	41.4	37.9
NCMA	1.20	0	76.7	23.3

* Obtained by the deconvolution of the CO_2 desorption curves.

coauthors [44] reported that CeO_2 + ZrO_2 solid solution at 1:4 Ce: Zr molar ratio showed total basicity lower than ZrO_2 and such property was only increased for Ce-enriched solid solutions, Ce: Zr = 1:1 and Ce: Zr = 4:1, in which ceria can be considered the zirconia acceptor oxide, that generates vacancies when associated to CeO_2, increasing the CO_2 adsorption capacity. The higher NZMA basicity could be also explained by a ZrO_2 partial phase transformation during the reducing process, which was taken before the CO_2 adsorption. As seen in the *in situ* XPD (Fig. S3), the monoclinic phase of zirconia was observed after the H_2 treatment at 750 °C. This phase appears at higher extent in NZMA catalyst, while ZrO_2 remains with a cubic and/or tetragonal structure in NCZMA catalyst. Pokroviski and coauthors [45] showed that the monoclinic zirconia features higher total basicity than the tetragonal phase. Considering that ZrO_2 is present in a greater amount than CeO_2 in NCZMA catalyst, the phase stabilization into cubic and/or tetragonal structure after H_2 exposure at 750 °C probably contributed more to the decrease of the total basicity than the lanthanide itself. Besides, it was discussed in XPS Section that the NZMA fresh catalyst featured higher Zr^{+x}/Zr^{+4} ratio than NCZMA, which produced more oxygen vacancies where CO_2 can be adsorbed on, and this may be extended to the catalyst after H_2 treatment, since the surface reduction of Zr^{+4} to Zr^{+3} can occur, as discussed in the H_2-TPR section. The highest Zr^{+x}/Zr^{+4} ratio featured by NZMA can also explain the largest participation (in %) of the base sites up to moderate strength, hindering the CO_2 adsorption on the strong sites, as reported by Debek and coauthors [11].

A significant increase in the catalyst basicity was only observed for NCMA. According to Daza and coauthors [26], ceria shows basicity properties only in presence of another alkaline metal, as Mg, which explains the increase of the NCMA catalyst total basicity. The CO_2 peaks desorption of the NCMA catalyst was also shifted to higher temperatures, indicating that CO_2 adsorption occurs distinctly in the presence of

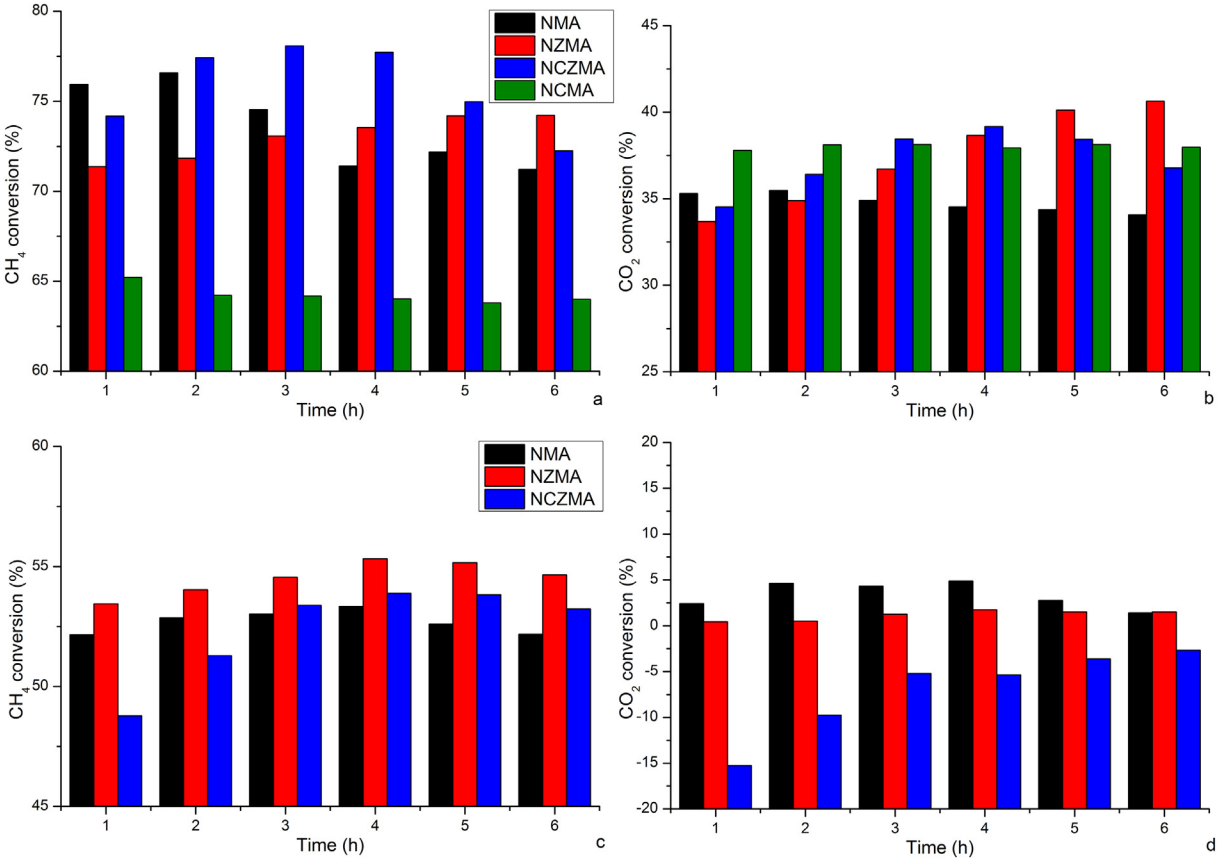

Fig. 9. CH_4 and CO_2 conversions at 750 °C (a and b) and 650 °C (c and d).

the rare earth oxide [15].

Among the catalysts studied, NZMA and NCMA showed the lowest strong basic sites concentration/participation (in %), *i.e.*, the presence of ZrO_2 or CeO_2 alone, promoted the CO_2 adsorption on sites up to moderate basic strength. In their studies, Debek and coauthors [11] showed that Zr presence hindered the CO_2 adsorption on the strong basic sites, since there was no peak related to these sites for zirconia promoted catalyst in the deconvolution curves presented in their work, while the Zr association to Ce favored the adsorption on these strong basic sites. The strong base sites, according to them [15], hindered the reaction between CO_2 and methane, enhancing the methane decomposition. Basic sites up to moderate strength nature (non-strong basic sites), distinctly from the strong natured sites, helps the carbon gasification, considering that once the CO_2 adsorption in the former is not too strong, the molecule is available to react with CH_4 more easily, avoiding the carbon accumulation produced by the hydrocarbon decomposition [11,15].

3.6. Catalytic tests

Fig. 9 shows the reactants percent conversions for the catalysts tested at 750 °C (a and b) and at 650 °C (c and d) in tri-reforming reaction. The O_2 conversion was complete for all catalysts at both temperatures.

A more unstable performance was observed for the NMA catalyst during the reaction at 750 °C. After 2 h on stream, CH_4 and CO_2 conversions decreased with NMA catalyst due to the carbon deposits, which covered the sites available for the reactants adsorption. In fact, this catalyst showed the highest carbon deposition among the catalysts evaluated at 750 °C, as summarized in Table 5. As for NZMA and NCZMA catalysts, CH_4 and CO_2 conversions were incremented. However, after 4 h, CH_4 conversion decreased from 77.7% to 72%, while CO_2, from 39% to 36.8%, for the NCZMA catalyst. Reactants conversions did not show any decreasing tendency along the 6 h of catalytic test for NZMA, whose conversions, especially CO_2, tended to increase with time. As shown in Table 5, the NZMA catalyst had the lowest carbon deposition, allowing the availability of the actives sites for new molecules adsorption and conversion. The lowest CH_4 conversion at 750 °C was obtained with NCMA, once the hydrocarbon decomposition reaction probably occurred in less extent with the Ce promoted catalyst compared to the other catalysts evaluated at this temperature. NCMA featured the smallest Ni^0 average particle size, as also summarized in Table 5, which are less reactive towards the CH_4 decomposition [46]. Thus, it led to the lowest amount of coke deposition, which was the same as presented by the NZMA catalyst. CO_2 conversion, on the other side, increased with NCMA, due to its greatest CO_2 adsorption capacity, as shown in the previous section, being the highest up to 4 h of reaction, when it was overcome by the NZMA CO_2 conversion.

The composition of the synthesis gas (H_2/CO) produced during the reaction at 750 °C was at around 2 (Table 5) with all the catalysts, except NCMA. The last one featured H_2/CO ratio of 1.8, explained by its lowest CH_4 conversion that implies in a stream less enriched in H_2, also leading to the lowest H_2 yield. Those values are suitable to the Fischer-Tropsch (FT) process [47]. According to Pakhare and Spivey [48] and Zhou and coworkers [49], the H_2/CO ratio produced during SRM (~3) is considered too high for the production of extended chains hydrocarbons. Despite POM also generates a syngas with a quality at around 2, safety issues must be considered, due to the exothermic characteristic of the reaction. As for DRM, the low H_2/CO ratio (~1) requires a water-gas shift reactor previous to FT process to adjust the syngas quality into the desired value [47].

Under the reaction conditions, all catalysts showed stability at 750 °C, mainly NZMA. Pino and coauthors [50] reported stable performance of the $Ce_{0.7}La_{0.2}Ni_{0.1}O_{2-x}$ catalyst along 150 h of tri-

Table 5
Products yields, syngas quality and carbon produced during TRM.*

Catalyst	Carbon deposition 750 °C–650 °C ($gC{\cdot}g_{cat}^{-1}{\cdot}h^{-1}$)	H_2/CO 750 °C–650 °C	Y_{H2} (%) 750 °C–650 °C	Y_{CO} (%) 750 °C–650 °C	Ni^0 average crystallite size (nm)*	Ni^0 average crystallite size after reaction (nm)*
NMA	0.011–0.021	2.0–2.3	66–46	61–37	16	18
NZMA	0.001–0.005	2.0–2.4	65–49	60–38	16	17
NCZMA	0.006–0.006	2.0–2.6	68–46	63–32	14.5	15
NCMA	0.001–n.e.	1.8–n.e.	55–n.e.	57–n.e.	7	8

n.e.—not evaluated at 650 °C.

* Calculated using Scherrer equation and 2θ = 52° Ni (200) reflection from *in situ* XPD patterns after reduction at 750 °C and after 2 h reaction at 750 °C.

reforming of methane reaction (T = 800 °C, GHSV = 31,000 h^{-1}), considering that it took 6 h to stabilize the process, in which period an increase of the reactants conversions could be observed until reaching stable values, which were kept during the 144 h. It was already discussed that the NZMA catalyst featured an increasing conversion trend along the 6 h of test.

NMA, NZMA and NCZMA catalysts were also tested at 650 °C to verify the temperature effect on TRM process. Obviously, conversions decreased. CO_2 conversions at 650 °C were close to zero in NMA and NZMA catalysts, once DRM does not occur at this condition and thus methane reacted mainly with water steam and oxygen. The absence of DRM at this temperature also explains the greater H_2/CO ratio than the produced during the reaction at 750 °C, once SRM and POM lead to higher H_2 concentrations [51]. "Negative" CO_2 conversion was also detected for NCZMA catalyst due to the CO_2 production, as consequence of the water-gas shift parallel reaction (WGS—reaction (7)) occurrence. This justifies the highest H_2/CO ratio and the lowest CO yield for NCZMA at 650 °C, as shown in Table 5 [49].

$$CO + H_2O \rightarrow H_2 + CO_2 \qquad \Delta H^0_{298K} = -41.2 \text{ kJ/mol} \tag{7}$$

In general, the carbon deposition in the catalytic sites was higher at 650 °C than at 750 °C, comparing the catalysts which were tested at the two temperatures. Carbon is produced mainly by CH_4 decomposition at 750 °C, and by CO disproportionation (Boudoard reaction) and CH_4 decomposition at 650 °C:

$$CH_4 \rightarrow C + 2H_2 \qquad \Delta H^0_{298K} = +74.9 \text{ kJ/mol} \tag{4}$$

$$2CO \rightarrow C + 2CO_2 \qquad \Delta H^0_{298K} = -172.2 \text{ kJ/mol} \tag{5}$$

NCZMA featured similar amounts of coke deposits at both reaction temperatures. This similarity may be explained by the gasification of the carbon species by water $C + H_2O \rightarrow CO + H_2$, which combined with reaction (5) results into the WGS (reaction (7)) at 650 °C.

The carbon amount deposition on the catalysts evaluated at 750 °C followed the trend: NMA > NCZMA > NZMA ~ NCMA. In general, this was the same tendency observed for the strong base sites concentration/participation (in %), shown in Table 4, and the inverse order of the reactants conversions, indicating that coke accumulation caused the decrease of the catalytic activity and it seems to be related to the percent participation of the strong base sites base sites. In other words, NMA, which presented the lowest non-strong (52%) and highest strong (48%) basic sites concentration, featured the highest amount of carbon deposits. On the other hand, NZMA and NCMA, which are the most non-strong basic sites enriched catalysts (72% and 76.7%, respectively), featured the lowest amounts of coke. The NCZMA is in an intermediate position in terms of non-strong basic sites concentration and carbon deposits. Thus, the carbon deposition seems to decrease as the non-strong basic sites participation (in %) increases and the strong concentration decreases.

According to Debek and coauthors [11,15], basic sites of strong nature hinder the reaction between CO_2 and CH_4. Thus, methane decomposes to carbon, which accumulates due to the lack of CO_2 for gasification. Similarly, Liu and coworkers [52] reported that strong base sites are not desired for the CO_2 conversion reactions. This result suggests that the types/strength of the basic sites and their participation on the catalyst basicity are relevant on determining the coke deposition. The greatest concentration of strong base sites (in %) in NMA catalyst led to an unstable performance, due to the CO_2 difficulty in reacting with CH_4, which increased the coke production and hindered the adsorption of new molecules on the unavailable coke covered sites. On the other side, NZMA featured the lowest percent concentration of these strong base sites, thus improving the performance along the 6 h on stream and minimizing coke deposition. Moreover, NZMA and NCMA presented the same amounts of carbon deposition, despite their average Ni^0 sizes, summarized in Table 5, being distinct. NCMA showed the smallest metallic particle size (7 nm), considering that small particles are less prone to the methane decomposition that generates carbon, as already discussed. Together with its greatest participation of non-strong base sites (76.7%), coke production could be minimized with the NCMA catalyst. It was discussed in the basicity properties section that non-strong natured basic sites (up to moderate strength) facilitate the reaction between CO_2 and CH_4, considering that the adsorption of the former molecule is not too strong on these sites, being available to react with the hydrocarbon. NZMA, on the other hand, featured a Ni^0 average particle size in the order of 16 nm. Particles of such sizes are usually subjected to coke production reactions, but considering that NZMA catalyst also showed one of the greatest participation of non-strong basic sites (71.9%), the gasification of coke deposits was probably benefited inducing kind of catalyst surface cleaning. These results can show that Ni particle size is not the only parameter that must be considered in reducing carbon deposition reactions; properties as the strength of the basic sites distribution can affect coke production.

The facts discussed previously can also explain the coke deposition at 650 °C, although CO_2 conversions at this temperature were close to zero. In this case, the basic sites strength allowed greater carbon gasification in NZMA and NCZMA than in NMA catalyst. Similarly, Özdemir and coauthors [31] attributed the low carbon deposition in POM reaction to appropriate basicity features.

NZMA and NCMA led to the lowest amounts of carbon deposits during TRM at 750 °C, but the increment of CH_4 and CO_2 conversions were observed with the former catalyst along the 6 h of test. In general, it can be said that the addition of Zr and Ce associated to Zr lowered the amount of carbon on the catalyst in TRM, without decreasing the total carbon conversion (CH_4 + CO_2). Besides, NCZMA catalyst also produced more H_2 and CO at 750 °C, as shows Table 5.

Majewski and Wood [51] studied the tri-reforming of methane at 750 °C employing a Ni/ SiO_2 (11% wt) catalyst and the following reactants composition: 1 CH_4:0.5 CO_2:0.5 H_2O:0.1 O_2. In this case, the gasifying agents, CO_2 and H_2O, are in excess in relation to methane. They found a carbon deposition equivalent to 5 $mgC{\cdot}g_{cat}^{-1}$ and 49 $mgC{\cdot}g_{cat}^{-1}$ after reaction at 750 °C and 650 °C, respectively. Under 1 CH_4:0.33 CO_2:0.47 H_2O:0.17 O_2 ratio, *i.e.* more drastic operation (only water steam is in excess), NZMA and NCMA carbon deposition was 6 $mgC{\cdot}g_{cat}^{-1}$ (0.001 $gC{\cdot}g_{cat}^{-1}{\cdot}h^{-1}$), which was the same order of magnitude of 5 $mgC{\cdot}g_{cat}^{-1}$. At 650 °C, NZMA and NCZMA featured a carbon deposition equivalent to 30 $mgC{\cdot}g_{cat}^{-1}$ (0.005 $gC{\cdot}g_{cat}^{-1}{\cdot}h^{-1}$)

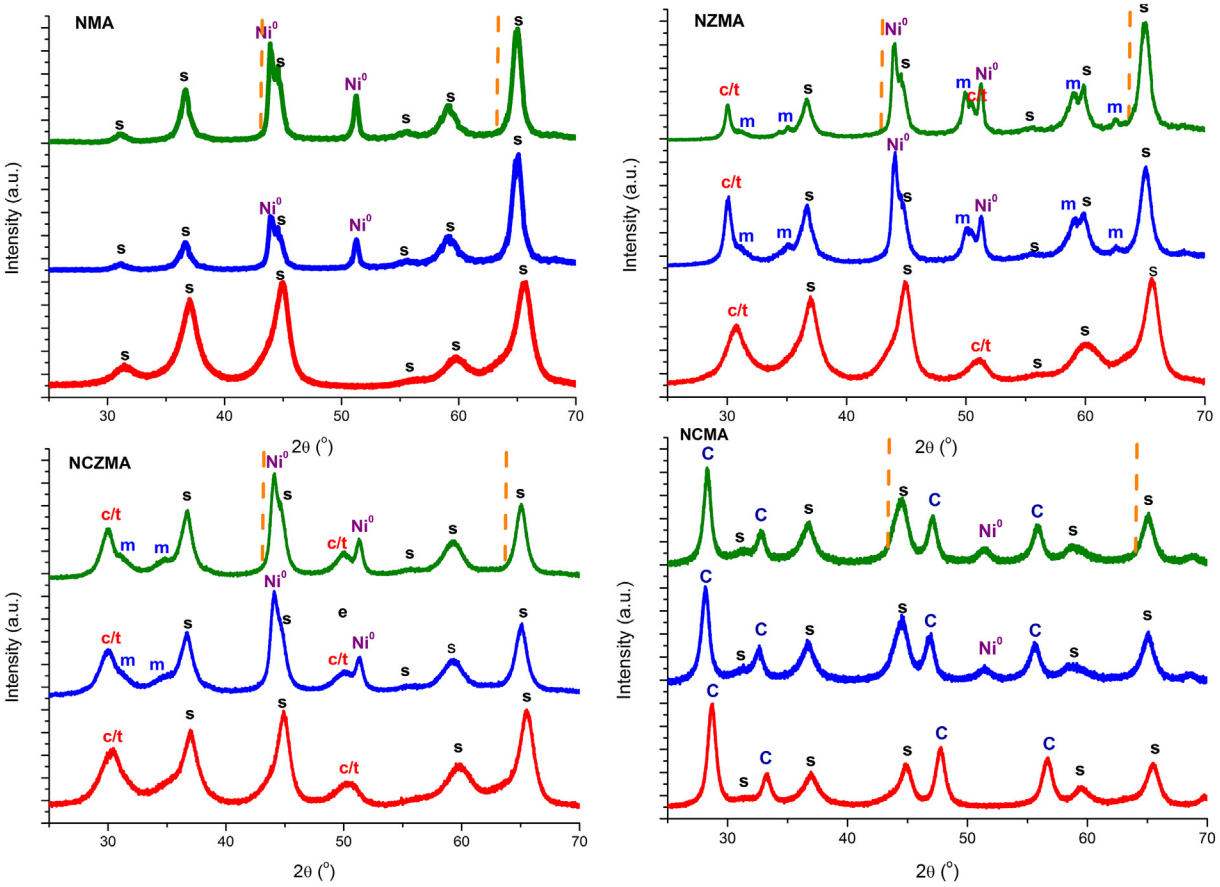

Fig. 10. NMA, NZMA, NCZMA and NCMA catalysts *in situ* XPD patterns. Red: fresh catalyst, blue: after reduction at 750 °C, green: after 2 h reaction at 750 °C. s—spinel, Ni—nickel metallic phase, c/t—cubic and/or tetragonal zirconia, dashed line: the position where NiO phase would be observed.

and 36 mgC·g_{cat}^{-1} (0.006 gC·g_{cat}^{-1}·h^{-1}), respectively, which was lower than the coke formation reported by these authors at the same reaction temperature and softer conditions (more CO_2 and water steam in the feed). Vita and coworkers [53] studied the tri-reforming of simulated biogas composition (1 CH_4:0.67 CO_2:0.3 H_2O:0.1 O_2) at 800 °C and found a carbon deposition equivalent to 0.11 gC·g_{cat}^{-1}·h^{-1} over a 7.7% (wt) Ni/CeO_2 catalyst, ten times greater than the NMA catalyst evaluated at 750 °C and almost twenty times greater than NCZMA tested at 650 °C, considering that carbon deposits are more likely to be produced at lower temperatures, due to the Boudoard reaction (reaction (5)).

XRD experiments were applied to track the catalysts changes in *in situ* and *in operando* conditions. Fig. 10 shows the *in situ* XPD patterns for the catalysts after activation and after 2 h of TRM reaction, both at 750 °C. The unstable zirconia monoclinic phase was mostly observed after reduction, as discussed in Section 3.5 (*Basicity properties*) and after reaction in NZMA pattern, as highlighted at the 2θ = 49–53° range (Fig. 11). The monoclinic ZrO_2 (JCPDS-02-0536) phase was also found in NCZMA catalyst, however in smaller extent compared to NZMA, showing Ce stabilized zirconia into cubic/tetragonal phase, even in H_2 atmosphere and under TRM operation.

The most important thing to be noticed is that none of the catalysts showed transformation from Ni^0 to NiO, which could happen due to the exposition to O_2 or even to H_2O, considering that one of the concerns about TRM is the loss of the active phase as a result from its oxidation by the gasifying agents [6].

3.7. Post-reaction characterizations

NMA and NCZMA showed filamentous carbon formation (Fig. S4) after reaction at 750 °C [54], while no carbon species was observed in the NZMA and NCMA spent catalysts micrographs at this reaction temperature. This result corroborates with the thermogravimetric analysis (Table 5), since the carbon deposition on the two catalysts was the lowest among the catalysts tested at 750 °C. SEM also showed higher carbon contents on the NMA spent catalyst surface among the catalysts tested at 650 °C, also in agreement with the TG analysis.

In the Raman spectra of the spent catalysts (Fig. 12), the D band at 1350 cm^{-1} is related to the defective/disordered filamentous carbon [55] and the G band arises from the sp^2 C—C stretching in hexagonal sheets, that is related to ordered and stable graphitic carbon species [56]. The D* shoulder is ascribed to some imperfection in these filamentous carbon [57]. NMA and NCZMA presented similar ratios between D and G bands intensities at 750 °C ($I_D/I_G \sim 1.18$), which express the disorder degree or graphitization of the carbonaceous species. The carbon material is graded as a disordered or defective structure when this ratio is close to unity [58]. Thus, the coke species produced from TRM at 750 °C could be considered disordered filamentous carbon deposits, as observed from the SEM images. This result was coherent with the DTG analysis (not shown): the spent catalysts presented the carbon removal peak close to 600 °C, associated to the filamentous carbon oxidation. Highly oriented carbon/graphitic species are associated to I_D/I_G ratio close to zero, and could only be burnt at temperatures higher than 675 °C [31,58]. NZMA and NCMA did not show any carbon band, confirming the lowest amount of coke deposited over these catalysts, as determined by TGA.

D and G bands could only be observed in the NZMA spent catalyst spectrum after the reaction at 650 °C (not shown), that corroborates with both SEM and TGA results. NMA and NCZMA carbon deposits disorder did not change with the decrease of the reaction temperature, suggesting the nature of the coke produced during the reaction at

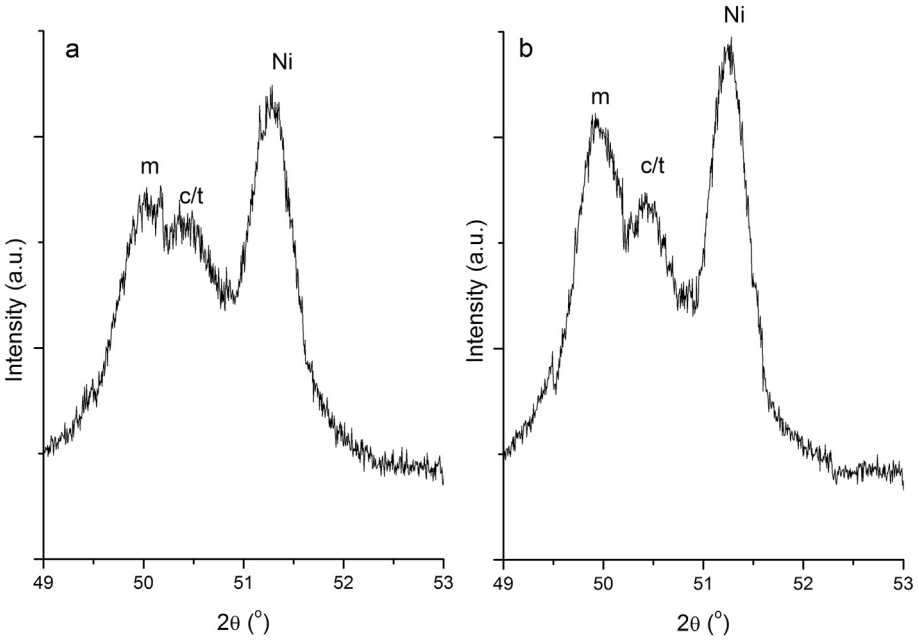

Fig. 11. NZMA XPD pattern approximation after reduction (a) and after reaction at 750 °C (b). Ni—nickel metallic phase, c/t—cubic and/or tetragonal zirconia.

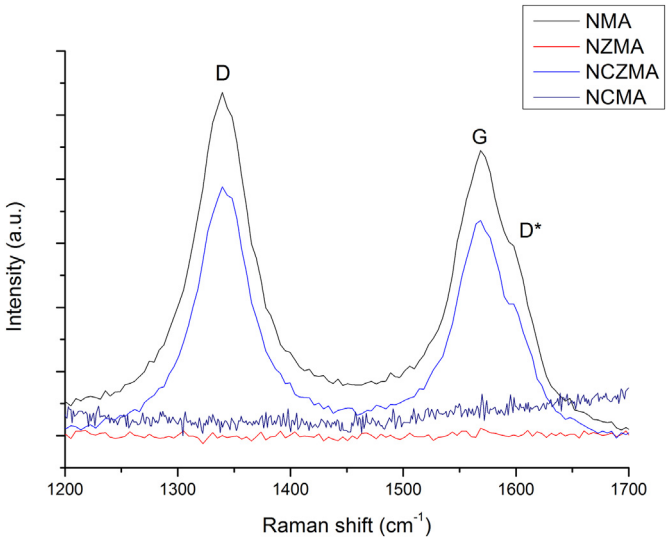

Fig. 12. Raman analyses of carbon species on spent catalysts at 750 °C.

650 °C was the same of those produced at 750 °C and the decrease of the reaction temperature increased the amount of coke deposition due to Boudoard reaction. Moreover, since all catalysts featured I_D/I_G ratios of 1.20 after reaction at 650 °C, it can be inferred that promoters did not change the nature of the carbon either, only influencing on the amount produced, which seems to be associated to the concentration (in %) of the basic sites of different strength, as discussed in the previous section.

4. Conclusions

The quality of the syngas (H_2/CO ratio) produced at 750 °C was near 2, suitable to Fischer-Tropsch process. In the catalysts evaluated at 750 °C, the amount of carbon deposits followed the order: NMA > NCZMA > NZMA ~ NCMA, which was the same trend observed for strong base sites concentration (in %). Despite NZMA and NCMA average Ni^0 sizes being distinct, they featured the same amounts of carbon deposits. Such occurrence can show the active phase particle size is not the only parameter that must be considered in reducing carbon deposition reactions, once the properties as the strength of the basic sites distribution can affect coke production. The non-strong natured basic sites (up to moderate strength) facilitate the reaction between CO_2 and CH_4, because the adsorption of the former molecule is not too strong on these sites, being available to react with the hydrocarbon. The smallest metallic particle size together with the greatest participation of non-strong base sites (76.7%) can explain the lowest carbon accumulation on the NCMA catalyst. NZMA presented a Ni^0 average particle size in the order of 16 nm. Particles of such sizes are usually subjected to coke production reactions, but once it also showed one of the greatest participation of non-strong basic sites (71.9%), the gasification of coke deposits was allowed through a kind of catalyst surface cleaning. Thus, it was concluded NZMA and NCMA catalysts led to the lowest amounts of carbon deposits during TRM at 750 °C, but the increment of CH_4 and CO_2 conversions were observed with the former catalyst along the 6 h of test. In general, the addition of Zr and Ce associated to Zr lowered the amount of carbon on the catalyst in TRM, without decreasing the total carbon conversion (CH_4 + CO_2). NZMA also showed the lowest amount of coke deposits among the catalysts that were evaluated at 650 °C, which can be related to the lowest concentration of the strong basic sites, favoring the carbon gasification. In general, Zr, Ce and Ce associated to Zr modified the distribution of the basic sites types (strength), thus contributing to reduce the amounts of coke on NMA, which were essentially disordered filamentous carbon type. The disordered nature of these carbon species suggests the unstable nature of the coke filaments, which can be easily gasified during the TRM.

Acknowledgments

The authors would like to thank São Paulo Research Foundation (FAPESP — grant 2014/25972-8) for the studentship and sponsorship support, Shell Brazil and FAPESP sponsorship through the Research Centre for Gas Innovation (RCGI grant 2014/50279-4), the Brazilian National Synchrotron Light Laboratory (LNLS) for the XPD experiments (Proposal 2016-0821). This study was financed in part by the Coordenação de Aperfeiçoamento de Pessoal de Nível Superior – Brasil (CAPES) – Finance Code 001.

Appendix A. Supplementary data

Supplementary data to this article can be found online at https://doi.org/10.1016/j.apsusc.2019.03.140.

References

[1] M.H. Rafiq, H.A. Jakobsen, R. Schmid, J.E. Hustad, Experimental studies and modeling of a fixed bed reactor for Fischer–Tropsch synthesis using biosyngas, Fuel Process. Technol. 92 (2011) 893–907.

[2] J.M. García-Vargas, J.L. Valverde, F. Dorado, P. Sánchez, Influence of the support on the catalytic behaviour of Ni catalysts for the dry reforming reaction and the tri-reforming process, J. Mol. Catal. A Chem. 395 (2014) 108–116.

[3] C. Song, W. Pan, Tri-reforming of methane: a novel concept for catalytic production of industrially useful synthesis gas with desired H_2/CO ratios, Catal. Today 98 (2004) 463–484.

[4] K.W. Jun, H.S. Roh, K.S. Kim, J.S. Ryu, K.W. Lee, Catalytic investigation for Fischer–Tropsch synthesis from bio-mass derived syngas, Appl. Catal. A Gen. 259 (2004) 221–226.

[5] D.M. Walker, S. Pettit, J.T. Wolan, J.N. Kuhn, Synthesis gas production to desired hydrogen to carbon monoxide ratios by tri-reforming of methane using Ni–MgO–(Ce,Zr)O_2 catalysts, Appl. Catal. A Gen. 445-446 (2012) 61–68.

[6] H. Jiang, H. Li, H. Xu, Y. Zhang, Preparation of Ni/$Mg_xTi_{1-x}O$ catalysts and investigation on their stability in tri-reforming of methane, Fuel Process. Technol. 88 (2007) 988–995.

[7] J. Guo, H. Lou, H. Zhao, D. Chai, X. Zheng, Dry reforming of methane over nickel catalysts supported on magnesium aluminate spinels, Appl. Catal. A Gen. 273 (2004) 75–82.

[8] H. Eltejaei, H.R. Bozorgzadeh, J. Towfighi, M. Omidkhah, M. Rezaei, R. Zanganeh, A. Zamaniyan, A.Z. Ghalam, Methane dry reforming on Ni/$Ce_{0.75}Zr_{0.25}O_2$–$MgAl_2O_4$ and Ni/$Ce_{0.75}Zr_{0.25}O_2$–γ-alumina: effects of support composition and water addition, Int. J. Hydrog. Energy 37 (2012) 4107–4118.

[9] R.K. Singha, A. Shukla, A. Yadav, S. Adak, Z. Iqbal, N. Siddiqui, R. Bal, Energy efficient methane tri-reforming for synthesis gas production over highly coke resistant nanocrystalline Ni–ZrO_2 catalyst, Appl. Energy 178 (2016) 110–125.

[10] S. Corthals, J.V. Nederkassel, J. Geboers, H. De Winne, J.V. Noyen, B. Moens, B. Sels, P. Jacobs, Influence of composition of $MgAl_2O_4$ supported $NiCeO_2ZrO_2$ catalysts on coke formation and catalyst stability for dry reforming of methane, Catal. Today 138 (2008) 28–32.

[11] R. Debek, M.E. Galvez, F. Launay, M. Motak, T. Grzybek, P. da Costa, Low temperature dry methane reforming over Ce, Zr and CeZr promoted Ni–Mg–Al hydrotalcite-derived catalysts, Int. J. Hydrog. Energy 41 (2016) 11616–11623.

[12] S.A. Shin, Y.S. Noh, G.H. Hong, J.I. Park, H.T. Song, K.Y. Lee, D.J. Moon, Dry reforming of methane over Ni/ZrO_2-Al_2O_3 catalysts: effect of preparation methods, J. Taiwan Inst. Chem. Eng. 000 (2017) 1–8.

[13] K.W. Koo, S.H. Lee, U.H. Jung, H.S. Roh, W.L. Yoon, Syngas production via combined steam and carbon dioxide reforming of methane over Ni–Ce/$MgAl_2O_4$ catalysts with enhanced coke resistance, Fuel Process. Technol. 119 (2014) 151–157.

[14] E.C. Faria, R.C.R. Neto, R.C. Colman, F.B. Noronha, Hydrogen production through CO_2 reforming of methane over Ni/$CeZrO_2$/Al_2O_3 catalysts, Catal. Today 228 (2014) 138–144.

[15] R. Debek, M.E. Galvez, M. Motak, T. Grzybek, P. da Costa, Influence of Ce/Zr molar ratio on catalytic performance of hydrotalcite-derived catalysts at low temperature CO_2 methane reforming, Int. J. Hydrog. Energy 42 (2017) 23556–23567.

[16] M.H. Youn, J.G. Seo, I.K. Song, Hydrogen production by auto-thermal reforming of ethanol over nickel catalyst supported on metal oxide-stabilized zirconia, Int. J. Hydrog. Energy 35 (2010) 3490–3498.

[17] F. Ocampo, B. Louis, L. Kiwi-Minsker, A.C. Roger, Effect of Ce/Zr composition and noble metal promotion on nickel based $Ce_xZr_{1-x}O_2$ catalysts for carbon dioxide methanation, Appl. Catal. A Gen. 392 (2011) 36–44.

[18] T. Shishido, M. Sokenobu, H. Morioka, M. Kondo, Y. Wang, K. Takaki, K. Takehira, CO_2 reforming of CH_4 over Ni/Mg–Al oxide catalysts prepared by solid phase crystallization method from Mg–Al hydrotalcite-like precursors, Catal. Lett. 73 (2001) 21–26.

[19] G. Leofanti, M. Padovan, G. Tozzola, B. Venturelli, Surface area and pore texture of catalysts, Catal. Today 41 (1998) 207–219.

[20] J. Wang, J. Zhou, Z. Li, Y. He, S. Lin, Q. Liu, M. Zhang, Z. Jiang, Mesoporous mixed metal oxides derived from P123-templated Mg–Al layered double hydroxides, J. Solid State Chem. 183 (2010) 2511–2515.

[21] B. Huang, C.H. Bartholomew, B.F. Woodfield, Improved calculations of pore size distribution for relatively large, irregular slit-shaped mesopore structure, Microporous Mesoporous Mater. 184 (2014) 112–121.

[22] Z. Jia, J. Wang, Y. Wang, B. Li, B. Wang, T. Qi, X. Wang, Nano-sheets with a large surface area and their application in electrochemical capacitors, J. Mater. Sci. Technol. 32 (2016) 147–152.

[23] S. Lu, Y. Liu, Preparation of meso-macroporous carbon nanotube-alumina composite monoliths and their application to the preferential oxidation of CO in hydrogen-rich gases, Appl. Catal. B Environ. 11-112 (2012) 492–501.

[24] Y.C. Lee, P.Y. Peng, W.S. Chang, C.M. Huang, Hierarchical meso-macroporous $LaMnO_3$ electrode material for rechargeable zinc-air batteries, J. Taiwan Inst. Chem. Eng. 45 (2014) 2334–2339.

[25] H. Mustu, S. Yasyerli, N. Yasyerli, G. Dogu, T. Dogu, P. Djinovic, A. Pintar, Effect of synthesis route of mesoporous zirconia based Ni catalysts on coke minimization in conversion of biogas to synthesis gas, Int. J. Hydrog. Energy 40 (2015) 3217–3228.

[26] C.E. Daza, S. Moreno, R. Molina, Co-precipitated NieMgeAl catalysts containing Ce for CO_2 reforming of methane, Int. J. Hydrog. Energy 36 (2011) 3886–3894.

[27] S.H. Kirumakki, B.G. Shpeizer, G.V. Sagar, K.V.R. Chary, A. Clearfield, Hydrogenation of naphthalene over NiO/SiO_2-Al_2O_3 catalysts: structure-activity correlation, J. Catal. 242 (2006) 319–331.

[28] B. Nematollahi, M. Rezaei, E.N. Lay, Preparation of highly active and stable NiO–CeO_2 nanocatalysts for CO selective methanation, Int. J. Hydrog. Energy 40 (2015) 8539–8547.

[29] A. Djaidja, S. Libs, A. Kiennemann, A. Barama, Characterization and activity in dry reforming of methane on NiMg/Al and Ni/MgO catalysts, Catal. Today 113 (2006) 194–200.

[30] J.E. Park, K.Y. Koo, U.H. Jung, J.H. Lee, H. Roh, W.L. Yoon, Syngas production by combined steam and CO_2 reforming of coke oven gas over highly sinter-stable La-promoted Ni/$MgAl_2O_4$ catalyst, Int. J. Hydrog. Energy 40 (2015) 13909–13917.

[31] H. Özdemir, M.A.F. Öksüzömer, M.A. Gürkaynak, Effect of the calcination temperature on Ni/$MgAl_2O_4$ catalyst structure and catalytic properties for partial oxidation of methane, Fuel. 116 (2014) 63–70.

[32] A.F. Lucrédio, G. Jerkiewickz, E.M. Assaf, Nickel catalysts promoted with cerium and lanthanum to reduce carbon formation in partial oxidation methane reactions, Appl. Catal. A Gen. 333 (2007) 90–95.

[33] A.R. González, Y.J.O. Asencios, E.M. Assaf, M. Assaf, Dry reforming of methane on Ni–Mg–Al nano-spheroid oxide catalysts prepared by the sol–gel method from hydrotalcite-like precursors, Appl. Surf. Sci. 280 (2013) 876–887.

[34] M. Montañez, R. Molina, S. Moreno, Nickel catalysts obtained from hydrotalcites by coprecipitation and urea hydrolysis for hydrogen production, Int. J. Hydrog. Energy 39 (2014) 8225–8237.

[35] J. Liu, P. Chen, L. Deng, J. He, L. Wang, L. Rong, J. Lei, A non-sulfited flower-like Ni-PTA catalyst that enhances the hydrotreatment efficiency of plant oil to produce green diesel, Nature (2015), https://doi.org/10.1038/srep15576.

[36] Q.L.M. Ha, U. Armbruster, H. Atia, M. Schneider, H. Lund, G. Agostini, J. Radnik, H.T. Vuong, A. Martin, Development of active and stable low nickel content catalysts for dry reforming of methane, Catalysts 7 (2017) 1–17, https://doi.org/10.3390/catal7050157.

[37] Y.S. Chen, J.F. Kang, B. Chen, B. Gao, L.F. Liu, X.Y. Liu, Y.Y. Wang, L. Wu, H.Y. Yu, J.Y. Wang, Q. Chen, E.G. Wang, Microscopic mechanism for unipolar resistive switching behavior of nickel oxides, J. Phys. D. Appl. Phys. 45 (2012) 1–6.

[38] H.J. Lee, D.C. Kang, S.H. Pyen, M. Shin, Y.W. Suh, H. Han, C.H. Shin, Production of H_2-free CO by decomposition of formic acid over ZrO_2 catalysts, Appl. Catal. A Gen. 531 (2017) 13–20.

[39] G. Pantaleo, V.L. Parola, F. Deganello, R.K. Singha, R. Bal, A.M. Venezia, Ni/CeO_2 catalysts for methane partial oxidation: synthesis driven structural and catalytic effects, Appl. Catal. B Environ. 189 (2017) 233–241.

[40] E. Paparazzo, G.M. Ingo, N. Zachetti, X-ray induced reduction effects at CeO_2 surfaces: an x-ray photoelectron spectroscopy study, J. Vac. Sci. Technol. A 9 (1991) 1416–1420.

[41] A.F. Lucrédio, J.D.A. Bellido, E.M. Assaf, Effects of adding La and Ce to hydrotalcite-type Ni/Mg/Al catalyst precursors on ethanol steam reforming reactions, Appl. Catal. A Gen. 388 (2010) 77–85.

[42] J.I. Di Cosimo, V.K. Díez, M. Xu, E. Iglesia, C.R. Apesteguía, Structure and surface and catalytic properties of Mg-Al basic oxides, J. Catal. 178 (1998) 499–510.

[43] A.H.M. Batista, F.S.O. Ramos, T.P. Braga, C.L. Lima, F.F. de Sousa, E.B.D. Barros, J.M. Filho, A.S. de Oliveira, J.R. de Sousa, J. Valentini, A.C. Oliveira, Mesoporous MAl_2O_4 (M = Cu, Ni, Fe or Mg) spinels: characterization and application in the catalytic dehydrogenation of ethylbenzene in the presence of CO_2, Appl. Catal. A Gen. 382 (2010) 148–157.

[44] M.G. Cutrufello, I. Ferino, R. Monaci, E. Rombi, V. Solinas, Acid-base properties of zirconium, cerium and lanthanum oxides by calorimetric and catalytic investigation, Top. Catal. 19 (2002) 225–240.

[45] K. Pokrovski, K.T. Jung, A.T. Bell, Investigation of CO and CO_2 adsorption on tetragonal and monoclinic zirconia, Langmuir. 17 (2001) 4297–4303.

[46] H.S. Bengaard, J.K. Norskov, J. Sehested, B.S. Clausen, L.P. Nielsen, A.M. Molenbroek, Steam reforming and graphite formation on Ni catalysts, J. Catal. 209 (2002) 365–384.

[47] A. Chiodini, L. Bua, L. Carnelli, R. Zwart, B. Vreugdenhil, M. Vocciante, Enhancements in biomass-to-liquid processes: gasification aiming at high hydrogen/carbon monoxide ratios for direct Fischer-Tropsch synthesis applications, Biomass Bioenergy 106 (2017) 104–114.

[48] D. Pakhare, J. Spivey, A review of dry (CO_2) reforming of methane over noble metal catalysts, Chem. Soc. Rev. (2013), https://doi.org/10.1039/c3cs60395d.

[49] C. Zhou, L. Zhang, A. SwiderskI, W. Yang, W. Blasiak, Study and development of a high temperature process of CH_4 with CO_2 or remediation of greenhouse gas, Energy. 36 (2011) 5450–5459.

[50] L. Pino, A. Vita, M. Laganà, V. Recupero, Hydrogen from biogas: catalytic tri-reforming process with Ni/La-Ce-O mixed oxides, Appl. Catal. B Environ. 148–149 (2014) 91–105.

[51] A.J. Majewski, J. Wood, Tri-reforming of methane over Ni/SiO_2 catalyst, Int. J. Hydrog. Energy 39 (2014) 12578–12585.

[52] H. Liu, L. Yao, H.B.H. Taief, M. Benzina, P. da Costa, M.E. Gálvez, Natural clay-based Ni-catalysts for dry reforming of methane at moderate temperatures, Catal. Today 306 (2016) 51–57.

[53] A. Vita, L. Pino, F. Cipitì, M. Laganà, V. Recupero, Biogas as renewable raw material for syngas production by tri-reforming process over $NiCeO_2$ catalysts: optimal operative condition and effect of nickel content, Fuel Process. Technol. 127 (2014) 47–58.

[54] A. Serrano-Lotina, A.J. Martin, M.A. Folgado, L. Daza, Dry reforming of methane to syngas over La-promoted hydrotalcite clay-derived catalysts, Int. J. Hydrog. Energy

37 (2012) 12342–12350.
[55] T. Xie, X. Zhao, J. Zhang, L. Shi, D. Zhang, Ni nanoparticles immobilized Ce-modified mesoporous silica via a novel sublimation-deposition strategy for catalytic reforming of methane with carbon dioxide, Int. J. Hydrog. Energy 40 (2015) 9685–9695.
[56] X. Lin, R. Li, M. Lu, C. Chen, D. Li, Y. Zhan, L. Jiang, Carbon dioxide reforming of methane over Ni catalysts prepared from Ni–Mg–Al layered double hydroxides: influence of Ni loadings, Fuel 162 (2015) 271–280.
[57] A. Serrano-Lotina, L. Daza, Highly stable and active catalyst for hydrogen production from biogas, J. Power Sources 238 (2013) 81–86.
[58] A. Serrano-Lotina, L. Rodríguez, G. Muñoz, A.J. Martin, M.A. Folgado, L. Daza, Biogas reforming over La-NiMgAl catalysts derived from hydrotalcite-like structure: influence of calcination temperature, Catal. Commun. 12 (2011) 961–967.